

Widespread land surface cooling from paddy rice cultivation revealed by global satellite mapping

Received: 28 May 2025

Accepted: 3 December 2025

Published online: 13 December 2025

 Check for updates

Wei Weng^{1,2,3}, Jingfeng Huang^{1,2,3}✉, Chao Yue^{4,5,6}, Zhenhao Lyu³, Yuanjun Xiao³, Shengcheng Li³, Ran Huang⁷, Dailiang Peng⁸, Chao Huang⁹, Florent Bigirimana¹⁰, Li Liu¹¹ & Weiwei Liu¹²

Paddy rice exacerbates climate warming through greenhouse gas emissions but also cools the land surface by enhancing evapotranspiration. While the former effect has received extensive attention, the biophysical cooling effect remains poorly quantified, partly due to the lack of high-quality global paddy rice data. Here, we address this gap by developing a universal rice mapping framework that integrates the strengths of phenology-based and curve-matching methods to construct the global, long-term rice dataset (GlobalRice500) with daily temporal and 500 m spatial resolution. Our analysis reveals that paddy fields annually reduce daytime land surface temperature by 0.21 (\pm 0.0057)–0.27 (\pm 0.0063) °C during the growing season compared to other croplands, with stronger cooling observed in larger fields and partial spillover to surrounding landscapes. These findings provide robust evidence of the surface cooling effect of paddy rice and call for a comprehensive evaluation of its role in climate regulation.

Paddy rice is not only a cornerstone of global food security but also influences the global climate in at least two distinct ways. On one hand, rice cultivation accounts for nearly 30% of global agricultural methane emissions¹ and ~48% of greenhouse gas emissions from croplands², contributing to global warming. On the other hand, paddy fields dissipate substantial heat through evapotranspiration³, which helps lower land surface temperature (LST). However, previous studies have focused on the former (warming)^{4–7} effect but completely overlooked the latter (cooling) effect, potentially leading to a skewed understanding of the overall climate impacts of rice ecosystems. Elucidating

the surface cooling effect of paddy fields is thus essential for a comprehensive assessment of their role in global climate regulation.

The global surface temperature effects of vegetation^{8,9} (e.g., forests^{10–12} and urban greening^{13,14}) and irrigation^{15,16} have been extensively studied. Although paddy fields consume approximately 30% of global irrigation water^{1,17} and represent a typical water–vegetation hybrid system, their cooling effect remains poorly quantified. The few existing studies are mostly limited to a relatively small geographic scope^{18–20}. One key limitation in addressing this knowledge gap is the lack of global rice distribution datasets with sufficient spatial and

¹State Key Laboratory of Soil Pollution Control and Safety, Zhejiang University, Hangzhou, China. ²Key Laboratory of Environmental Remediation and Ecological Health, Ministry of Education, Zhejiang University, Hangzhou, China. ³Institute of Applied Remote Sensing and Information Technology, Zhejiang University, Hangzhou, China. ⁴College of Natural Resources and Environment, Northwest A&F University, Yangling, China. ⁵State Key Laboratory of Soil and Water Conservation and Desertification Control, Northwest A&F University, Yangling, China. ⁶Institute of Soil and Water Conservation, Northwest A&F University, Yangling, China. ⁷School of Automation, Xiasha Higher Education Zone, Hangzhou Dianzi University, Hangzhou, China. ⁸Key Laboratory of Digital Earth Science, Aerospace Information Research Institute, Chinese Academy of Sciences, Beijing, China. ⁹Key Laboratory of National Forestry and Grassland Administration on Forest Ecosystem Protection and Restoration of Poyang Lake Watershed, College of Forestry, Jiangxi Agricultural University, Nanchang, China. ¹⁰National Institute of Statistics of Rwanda, Kigali, Rwanda. ¹¹College of Computer and Information Technology, China Three Gorges University, Yichang, Hubei, China. ¹²Department of Geography and Spatial Information Techniques, Ningbo University, Ningbo, China.

✉ e-mail: [hjfh@zju.edu.cn](mailto:hjf@zju.edu.cn)

temporal resolution. As a comparison, forests typically exhibit long-term land cover continuity and relatively regular seasonal patterns. In contrast, paddy fields are subject to intensive human management, which often results in frequent land use changes and irregular seasonal dynamics. Such variability arises from practices such as crop rotation, temporary fallowing, or land conversion, as well as from the flexibility in planting schedules. In tropical regions, where water and heat are available year-round, rice can be cultivated at almost any time of the year. These characteristics make paddy fields especially challenging to monitor. Unlike forests, which can often be described using annual or multi-year averages, paddy fields require much higher temporal resolution to accurately capture the start, end, and duration of the rice growing season and to quantify their surface biophysical effect.

Considerable efforts have been made to map global rice area using satellite remote sensing since 2004 (Supplementary Table 1). However, to the best of our knowledge, none of the existing rice maps simultaneously satisfy the multiple requirements of global coverage, moderate spatial resolution, long temporal coverage and high temporal resolution. Most available datasets have a temporal resolution no higher than annual, with the exception of MIRCA2000²¹ and GAEZ + _2015²², which are monthly. Global-scale maps typically offer coarse spatial resolution (>5 km)^{23,24}, and are often limited to a single year of temporal coverage, with the exception of GDHY^{25–27}. Higher spatial resolution maps generally have limited spatial coverage and are predominantly available for more developed regions^{28,29}, leaving data gaps in less-developed areas such as Africa, Central and West Asia.

Here, we construct a spatially and temporally comprehensive global rice dataset to assess the role of paddy rice in regulating land surface temperature. We address major bottlenecks in rice mapping caused by the variability in rice planting times and the deficiency of prior knowledge. We develop a universal rice mapping framework that identifies the start and end of the rice growing season on a daily basis, capable of recognizing paddy rice with arbitrary durations and intensities. This framework underpins the creation of GlobalRice500, a global-scale, long-term dataset of rice planting area with daily temporal and moderate spatial resolution. Finally, we analyze the cooling effect of paddy fields and characterize its spatial and temporal patterns, complemented by an uncertainty assessment to ensure the robustness of the results. Our findings offer a perspective and contribute to a more comprehensive understanding of the role of rice ecosystems in global climate regulation.

Results

The construction of GlobalRice500: long term mapping of global rice planting area

We first address the key bottlenecks in rice mapping by developing a universal rice mapping framework that integrates Moving Phenological Detection and Dynamic Time Warping (MPD_DTW³⁰, Fig. 1). MPD_DTW identifies the start and end of rice growing season on a daily basis, enabling the recognition of paddy rice with arbitrary growth durations and intensities. By leveraging the concept of “moving detection”, the MPD_DTW framework combines the dual strengths of

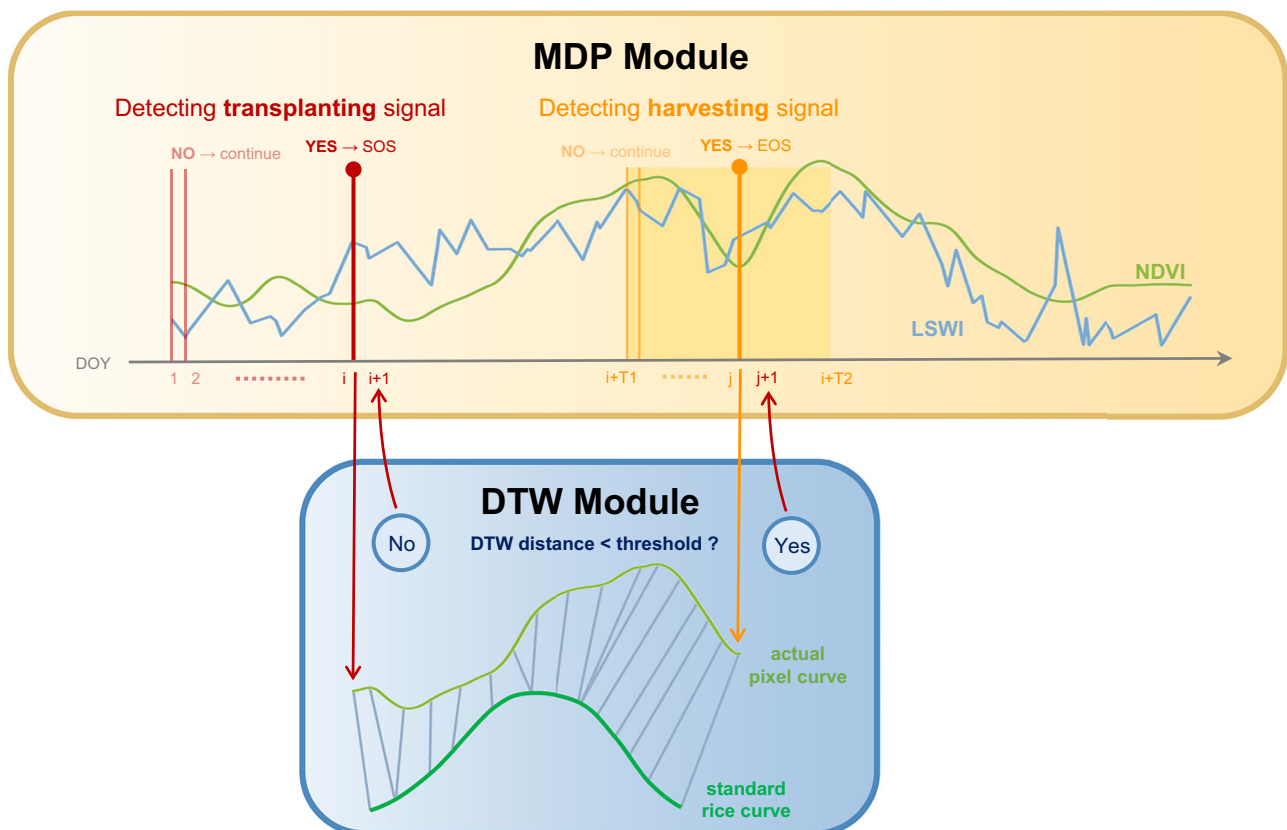


Fig. 1 | Schematic diagram of Moving Phenological Detection and Dynamic Time Warping (MPD_DTW). The diagram illustrates the workflow for identifying rice growing seasons based on daily time series data. The MPD module detects the start (SOS) and end (EOS) of the rice growing season (RGS) based on phenological knowledge. Thin vertical lines without solid circles denote days that do not meet the identification conditions, whereas thick vertical lines with solid circles indicate days that do. EOS is searched after the identified SOS (denoted as i in the figure), within a search window from $i + T1$ to $i + T2$ (yellow block), which corresponds to

the locally defined rice growth duration. The NDVI curve within the detected SOS–EOS period (i to j) is then analyzed by the DTW module to determine whether the time period corresponds to a RGS. The DTW module subsequently provides feedback to the MPD module, specifying the starting day for detecting the next SOS. If the current curve is recognized as a RGS, the next SOS detection starts from the day after the current EOS ($j + 1$), ensuring no temporal overlap between consecutive seasons. Otherwise, the SOS detection restarts from the day following the current SOS ($i + 1$).

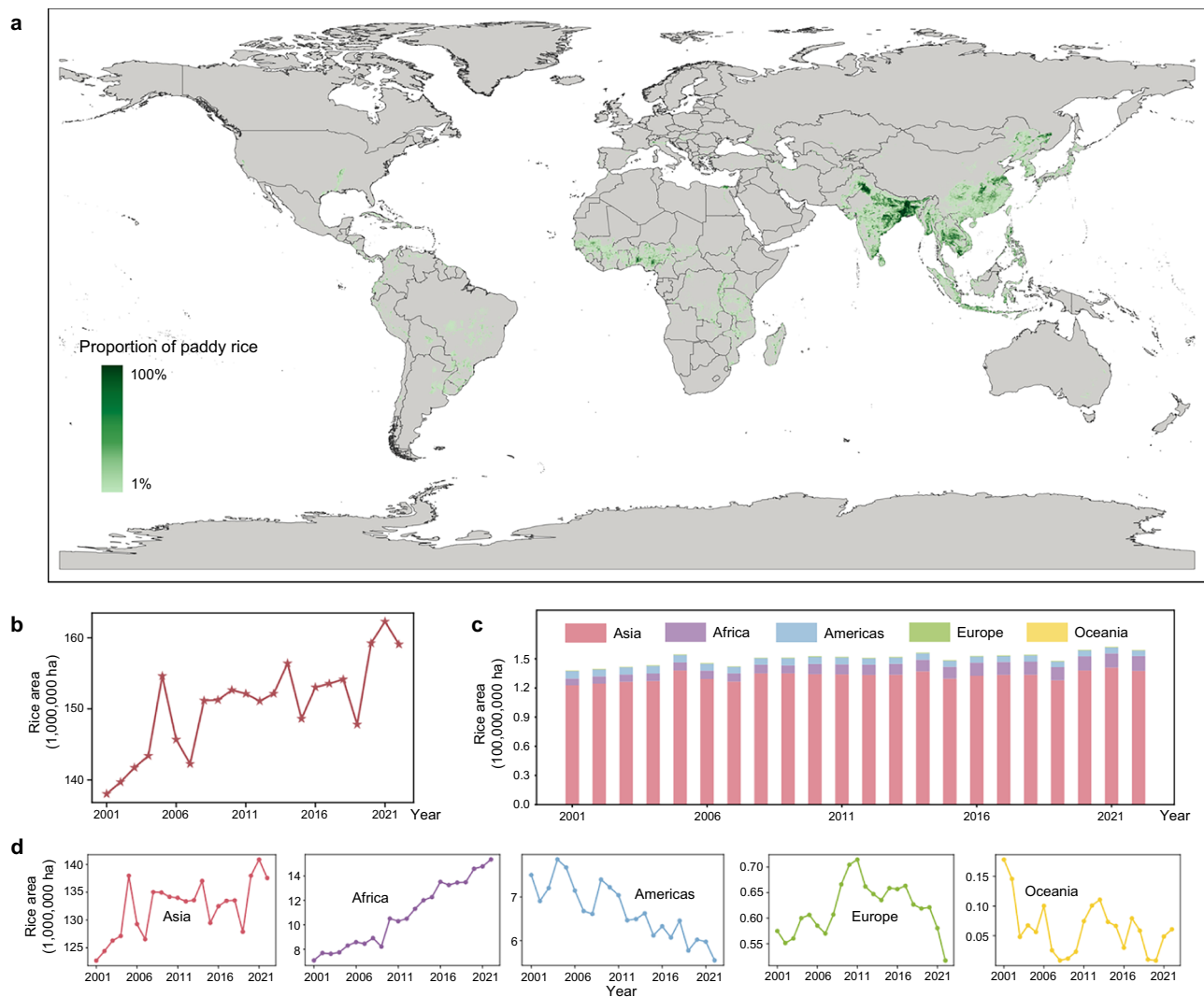


Fig. 2 | Long-term mapping of global paddy fields. **a** Global rice area in 2022, presented as proportions within 10 km × 10 km grids. **b** Temporal variations in global rice area. **c** Continental shares of rice areas. **d** Temporal variations for

different continents. All panels are derived from GlobalRice500. Raw data to reproduce **b–d** are provided as source data.

both phenology-based and curve-matching methods. This approach has the advantage to go beyond rice mapping to offer inspiration for mapping other crops with distinct phenological phases, such as winter wheat characterized by a green-up stage.

We applied the MPD_DTW to analyze over 40 terabytes of satellite imagery spanning 2000–2023 and created GlobalRice500³¹—the global-scale, long-term coverage (2001–2022), daily temporal resolution, 500 m spatial resolution dataset of rice planting area (Fig. 2a). Since 2001, the global rice area has exhibited a fluctuating upward trend (Fig. 2b), with a net expansion of over 21 million hectares by 2022. Spatially, rice cultivation is primarily concentrated in Asia, with additional distribution found in Africa, North America, South America, Europe, and Oceania (Fig. 2c). From 2001 to 2022, Asia remained the world’s dominant rice-growing continent, accounting for >85% of the global rice area (Fig. 2c). Africa, now the second-largest rice-growing continent, recorded the fastest growth in rice area among all continents, more than doubling its area since the early twenty-first century (Fig. 2d). In contrast, the Americas experienced a notable decline (Fig. 2d). Driven by abundant heat and water availability, equatorial regions showed a higher propensity for rice cultivation (Fig. 2a). Aside from two leading rice-producing giants, India (ranked first) and China (ranked second), most of the

other top countries with the largest rice areas were also located in tropical and subtropical regions (Fig. 3a).

For reference, we compiled existing local-scale high-resolution rice maps from diverse sources, including publicly available governmental datasets and rice maps released by academic researchers. The reference datasets cover all rice-growing continents and capture the diversity of global cultivation systems such as single-, double-, and multi-cropping (Supplementary Table 2). The overall accuracies typically exceed 90%, except in southeastern China, where it reached 88.85% (Fig. 3a and Supplementary Table 3). Moreover, comparison of country-level rice area between GlobalRice500 and FAO statistical data for 113 countries revealed a high degree of consistency, with an R-squared value of 0.98 (Fig. 3b). The spatial distribution of paddy rice derived by GlobalRice500 also aligned well with existing high spatial resolution rice maps (Fig. 3c–e).

The global cooling effect of paddy fields

The daily temporal resolution of GlobalRice500 enables precise delineation of rice growing seasons across diverse cropping systems worldwide, which is essential for quantifying the surface biophysical effect of paddy cultivation. This cooling effect by paddy rice is manifested in the reduction of land surface temperature (LST)¹¹, which is

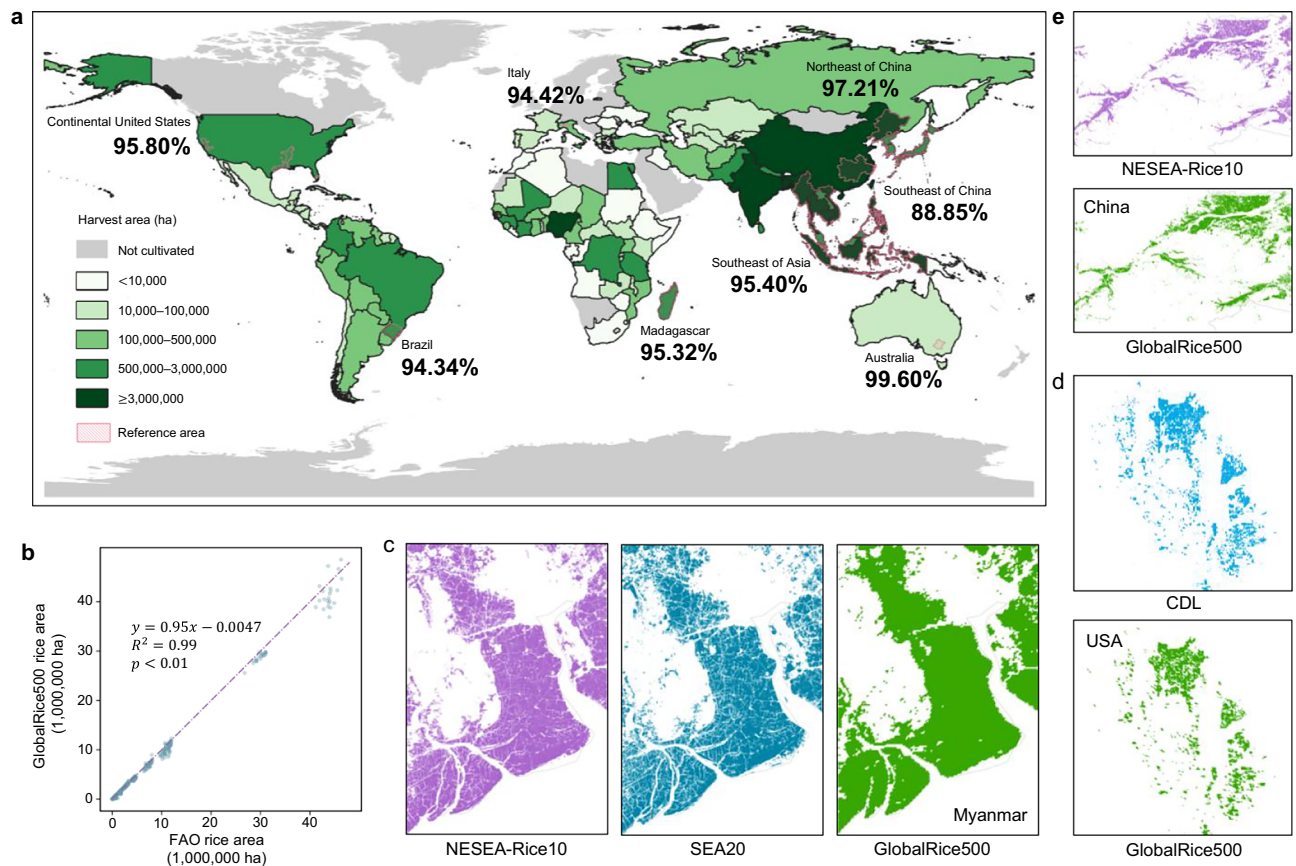


Fig. 3 | Validations of GlobalRice500. **a** Overall accuracies of GlobalRice500 across nine reference regions compared with satellite-derived rice maps. **b** Comparison of GlobalRice500 and FAO country-level statistics for 113 countries (2001–2022), where each dot represents a country–year observation. **c–e** Visual comparison of rice spatial distribution between high-resolution rice maps and the

–500 m GlobalRice500 for Myanmar (2019; 96.1°E, 16.6°N) (**c**), the USA (2022; 121.8°W, 39.1°N) (**d**) and China (2019; 130.6°E, 46.4°N) (**e**). High resolution rice maps include the 10 m NESEA-Rice10⁵⁷, the 20 m SEA20⁵⁸ and the 30 m Cropland Data Layer (CDL)⁵⁹. Raw data to reproduce (**b**) are provided as source data.

measured as the difference in LST (Δ LST) between non-paddy croplands and paddy fields during the rice growing season (see “Methods”). Our findings demonstrate that rice cultivation exerts a widespread cooling effect on the Earth’s surface. Globally, the annual mean daytime Δ LST between non-paddy croplands and paddy fields during 2003–2020 fluctuated between 0.21 (± 0.0057) °C and 0.27 (± 0.0063) °C (Fig. 4a). In contrast, the nighttime Δ LST was much smaller and nearly negligible—typically close to zero—indicating that the nighttime LST of paddy fields closely resembles that of surrounding non-paddy croplands (Figs. 4b and 5b). Uncertainty analyses of annual means for daytime and nighttime are reported in Supplementary Tables 4 and 5, respectively. During the rice growing season, daytime Δ LST exhibited an inverted V-shaped pattern with time, reaching its maximum value around Day of Season (DOS) 60–100 (Fig. 5c), largely corresponding to the peak growth stage.

We quantified the relationship between daytime Δ LST and paddy proportion (Methods) within 10-km grids and found that regions with higher paddy proportions exhibited stronger cooling effects (Fig. 5a). Regression analysis showed that Δ LST increased by approximately 0.0014 °C for every 1% increase in paddy proportion. Daytime Δ LST was further analyzed across different paddy field sizes, revealing that larger paddy fields tended to exhibit stronger cooling (Fig. 5b–d). Specifically, the maximum Δ LST during the rice growing season increased from 0.18 (± 0.0032) °C at size 1 to 0.69 (± 0.042) °C at size 11 (Fig. 5c).

To further investigate the spatial extent of the cooling influence, surrounding non-paddy areas were divided into concentric square-

shaped rings according to their distances from the paddy fields, termed non-paddy ladders (NPLs) (Methods). Regardless of paddy field size, NPLs closer to paddy fields consistently showed lower Δ LST, which gradually increased and stabilized when moving further away from the paddy fields (Fig. 5d). This pattern indicates that the cooling effect of paddy rice extends beyond paddy field boundaries and spills over into surrounding non-paddy areas. Such spillover cooling suggests that paddy fields may contribute to local land surface temperature reduction³², potentially mitigating urban heat island effects in adjacent cities^{33,34}. To mitigate the spillover effect of paddy field cooling, NPL₀₋₉ was excluded in the calculation of Δ LST in Fig. 4 and Fig. 5a–c, with non-paddy areas represented by NPL₁₀₋₃₀ (Methods).

Discussion

Our first goal is to develop a universal crop identification framework adaptable across diverse crop varieties, agro-climatic regions, and cropping systems. The proposed MPD_DTW framework leverages the idea of “moving detection” to integrate the strengths of phenology-based and curve-matching methods while mitigating their respective limitations. Its demonstrated spatial and temporal transferability in global, long-term rice mapping underscores its robustness. While NDVI and LSWI effectively capture flooding and greening dynamics in many paddy rice systems, they may underperform in regions with atypical water-management regimes and in dry direct-seeded systems, where flooding signals are often weak or absent. Moreover, although the 500 m spatial resolution of GlobalRice500 marks an advance over most existing global rice maps (>5 km, Supplementary Table 1), mixed-

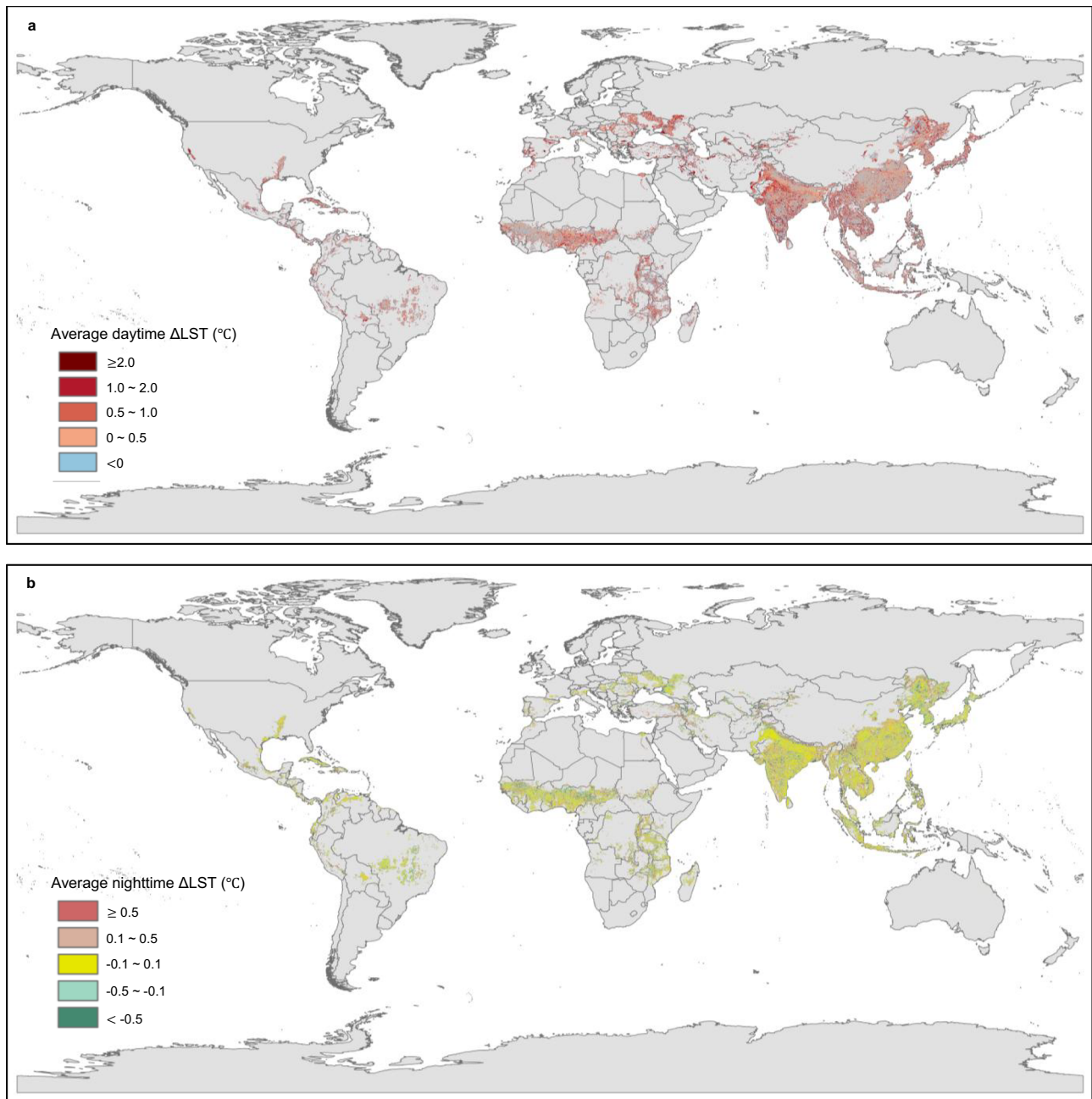


Fig. 4 | Global cooling effect of paddy fields. Geospatial distribution of mean daytime (a) and nighttime (b) land surface temperature difference (Δ LST) during 2003–2020, displayed as averages within 10 km \times 10 km grids. Δ LST indicates the

difference in LST between non-paddy croplands and paddy fields (non-paddy minus paddy) during the rice growing season.

pixel effects cannot be entirely avoided, as a single pixel may encompass multiple land-cover types, leading to spectrally mixed signals and reduced classification accuracy. Small, fragmented, and heterogeneous rice plots are particularly difficult to delineate accurately, whereas large, contiguous paddies can be mapped with greater confidence.

Statistical data (e.g., FAO) and satellite-derived observations (e.g., GlobalRice500) possess distinct advantages and limitations, yet their complementary strengths can be leveraged to provide a more comprehensive understanding of the global rice distribution. Building on this complementarity, our evaluation of GlobalRice500 integrates both perspectives: FAO statistics provide aggregated national or regional totals useful for benchmarking large-scale, long-term consistency, whereas satellite-derived maps deliver fine-scale spatial

details over specific periods, essential for characterizing local heterogeneity. However, our validation based on existing satellite-derived maps may exhibit spatial and temporal unevenness. Since Asia accounts for more than 85% of the global rice-harvested area and exhibits diverse cultivation systems, validation in this region is more extensive and detailed than in other regions. Moreover, existing high-resolution rice maps are generally limited in temporal and/or spatial coverage (Supplementary Table 1), resulting in an uneven and incomplete validation scope. This limitation further underscores the motivation for, and contribution of, producing the global, long-term rice dataset, GlobalRice500.

Our analysis provides the global assessment of the cooling effects of paddy fields on land surface temperature. The cooling effect of paddy rice stems primarily from the redistribution of the absorbed

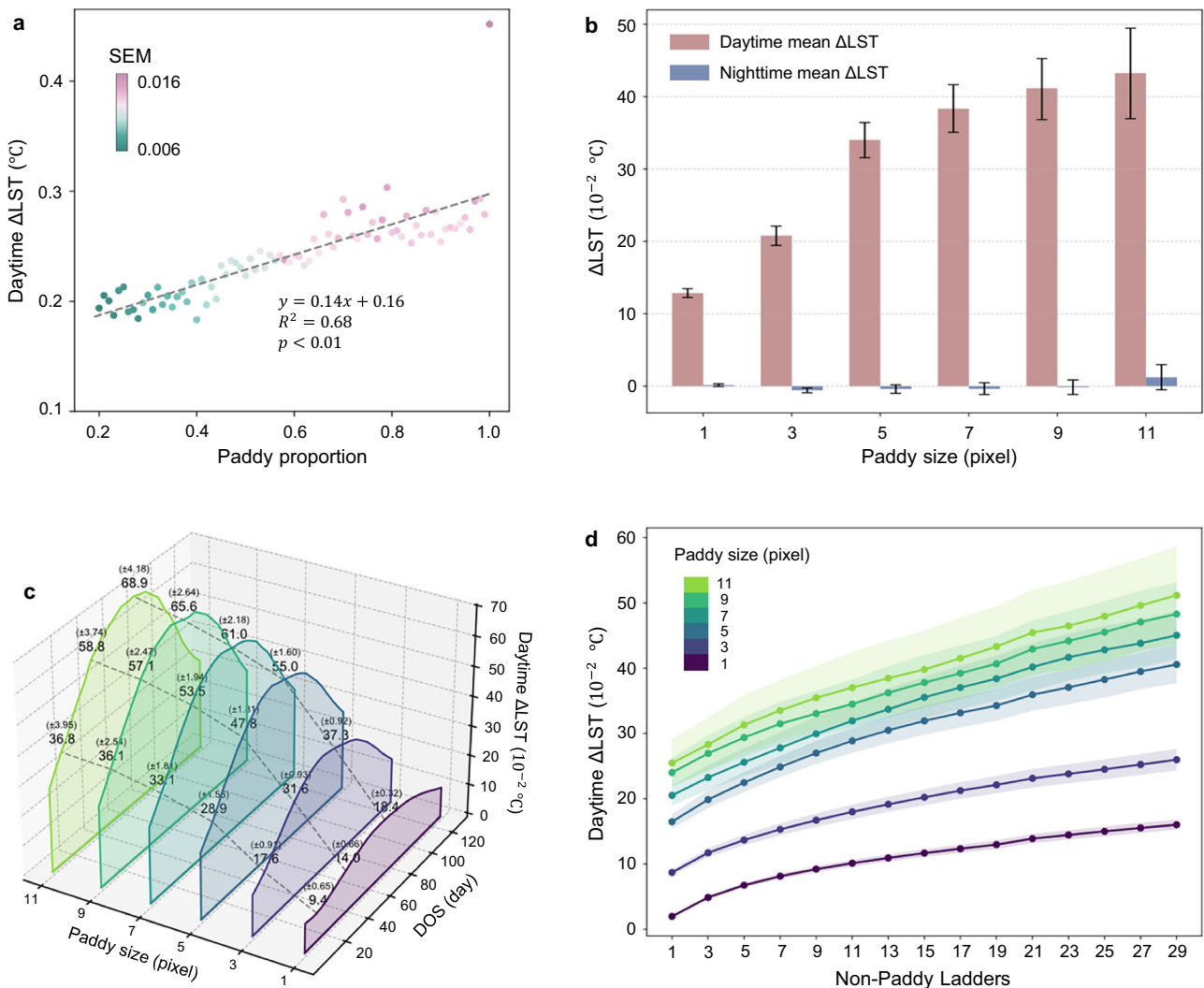


Fig. 5 | Multidimensional variations of land surface temperature difference (ΔLST). **a** Relationship between ΔLST and paddy proportion (Methods). Marker color indicates the standard error of the mean (SEM). **b** Variations in ΔLST with paddy field size. Red indicates daytime means and blue indicates nighttime means. Paddy size is represented by the side length (in pixels) of the paddy fields; for example, a value of 5 denotes paddy fields measuring 5 × 5 pixels. Error bars indicate 95% confidence intervals (95% CIs). **c** Seasonal variations of ΔLST across

different Days of Season (DOS) for paddy fields of varying sizes, with curves smoothed using a five-day moving average. Numbers in parentheses indicate SEM. **d** Spillover effect of paddy field cooling. The number *k* on the horizontal axis denotes the subscript of NPL_{*k*} (Methods). Different colors indicate paddy fields of varying sizes. Lines with markers show the means; shaded ribbons indicate the 95% CIs. Raw data to reproduce this figure are provided as source data.

solar energy through evapotranspiration²⁰, which includes both evaporation of surface water and plant transpiration. This process converts incoming solar radiation into latent heat, reducing the amount of sensible heat that would otherwise increase LST. At night, solar radiation drops to zero and evapotranspiration decreases substantially, explaining the negligible effect on LST (Figs. 4b and 5b), which is consistent with previous findings¹⁹.

To ensure a comparable background, the non-paddy croplands serving as the control group were carefully selected under multiple constraints (Methods)^{8,11,35}. Nevertheless, some determinants of LST cannot be fully constrained in an observational design, and residual differences in broadband albedo, soil moisture, and irrigation infrastructure may still have influenced our estimates. Additionally, the LST dataset used predominantly represents clear-sky rather than all-weather conditions³⁶. As it is derived from MODIS, retrievals rely on assumptions about atmospheric profiles and surface emissivity, and residual biases may arise under aerosol or thin-cloud contamination or over heterogeneous terrain³⁷. Finally, combining 1 km LST with 500 m rice maps inevitably entails a change of support; mixed-pixel and

adjacency effects can introduce bias and attenuate field-scale LST gradients.

Given that the accuracy of satellite-derived LST retrievals varies by climate³⁶, we further conducted a sensitivity analysis by stratifying ΔLST by Köppen–Geiger climate zones (2017)³⁸. Zone-level means were summarized with 95% confidence intervals (CIs) and standard errors (SEs) (Supplementary Table 6). The SEMs were consistently small and the CIs were narrow across climate zones, indicating that, despite potential retrieval biases, the observed cooling effect of paddy fields remains statistically robust.

Among different land-use and land-cover types, afforestation has been reported to induce local cooling of 0.07–1.16 °C³⁹. Satellite-based analyses further demonstrate that the LST effects of forests vary by forest type and latitude—showing cooling of 0.27 ± 0.03 °C in mid-latitudes, 0.50 ± 0.19 °C in southern high latitudes, and 2.41 ± 0.10 °C in tropical forests, but warming of 0.79 ± 0.03 °C in boreal forests¹¹. By contrast, our results indicate that daytime mean cooling ranges from 0.13 ± 0.03 °C in smaller (–500 m × 500 m) paddy fields to 0.43 ± 0.03 °C in larger (–5.5 km × 5.5 km) ones. It is worth noting that

the forest-related cooling reported above is measured relative to openlands, whereas our estimates are referenced to non-paddy croplands. Despite the smaller magnitude, the paddy-induced cooling represents a significant biophysical signal for an intensively managed and spatially fragmented agroecosystem.

As water-rich agroecosystems, paddy fields exert contrasting effects: abundant standing water enhances evapotranspiration and induces local cooling, whereas persistent flooding creates anaerobic conditions that stimulate methanogenesis, thereby increasing methane (CH₄) emissions². According to the IPCC Sixth Assessment Report (AR6), the best estimate of the total human-caused increase in global mean surface air temperature (GSAT) from 1850–1900 to 2010–2019 is 1.07 °C⁴⁰. Global rice cultivation contributes approximately 2.5% to present-day anthropogenic warming⁴¹, corresponding to a GSAT contribution of about 0.03 °C. These GSAT-based estimates reflect the global, multi-decadal accumulation of atmospheric heat driven by greenhouse gases, whereas our LST-based results quantify the global mean biophysical response of surface energy fluxes, primarily driven by local evapotranspiration from paddy fields. Although our results reveal that paddy fields exhibit an annual mean cooling of 0.21–0.27 °C relative to other croplands, it is important to note that they occupy only about 1% of the global land surface⁴². Future studies should harmonize these temperature metrics to better quantify the integrated climate impact of paddy cultivation.

These findings have broader implications for global climate policy. While greenhouse gas mitigation remains the primary objective for reducing anthropogenic warming, the biophysical cooling of paddy agroecosystems should also be recognized as a local adaptation co-benefit⁴³. Previous studies have shown that vegetation greening can induce a net cooling effect on surface air temperature through enhanced evapotranspiration, partly offsetting greenhouse-gas-driven warming⁴⁴. By quantifying the biophysical cooling effects of paddy ecosystems, our study provides a complementary basis for refining climate modeling and informing more balanced, climate-responsive agricultural strategies. At the field scale, such strategies could leverage the local cooling of paddy fields to buffer heat stress on crops and farm labor, thereby moderating hot-spot temperatures during the growing season. In many regions, dryland crops in low-lying areas often suffer from waterlogging during heavy rainfall, whereas these same areas are naturally suited for paddy cultivation, which can better utilize the standing water and mitigate heat stress. Where water availability allows, maintaining paddy in heat-prone subregions could be considered to harness these microclimate benefits, though such measures must be carefully evaluated in light of greenhouse gas and water management trade-offs.

Methods

Data sources and preprocessing

In this study, all available 500 m 8-day Moderate Resolution Imaging Spectroradiometer (MODIS) surface reflectance products from 2000 to 2023 were utilized to extract land surface information. Normalized Difference Vegetation Index (NDVI) and Land Surface Water Index (LSWI) were calculated from surface reflectance using the following formulas, and recorded their Days of Year (DOYs) in the meantime.

$$\text{NDVI} = \frac{\text{NIR} - \text{R}}{\text{NIR} + \text{R}} \quad (1)$$

$$\text{LSWI} = \frac{\text{NIR} - \text{SWIR}}{\text{NIR} + \text{SWIR}} \quad (2)$$

where R, NIR, SWIR represent the band of red (620–670 nm), near infrared (841–876 nm), short-wave infrared (2105–2135 nm), respectively. NDVI could reflect crop biomass and chlorophyll content, since it's correlated with leaf area index (LAI), green biomass, and percent

green vegetation cover⁴⁵. LSWI is sensitive to the total amount of liquid water in vegetation and its soil background⁴⁶, so it has been widely used to identify flooding signals during rice transplanting period. Maximum synthesis of NDVIs from MOD09A1 and MYD09A1 was then performed each 8-day interval, in order to reduce the contamination of clouds and rain. Since the sensitivity of flooding signals is crucial for rice mapping, all the available LSWIs were retained⁴⁷. To acquire daily VIs, we applied a Savitzky-Golay filter⁴⁸ to the NDVIs and a linear interpolation to the LSWIs.

To improve mapping efficiency and accuracy, Land Cover (LC) Products were added to mask out non-cropland area. We selected three LC products: IGBP (MCD12Q1 Land Cover Type 1) from 2001 to 2022, GlobeLand30⁴⁹ in 2010 and Crop Data Layer (CDL) in 2008–2022. GlobeLand30 and CDL were resampled into the format of 500 m MODIS tiles, and pixels with cropland no less than 50% were reserved. Resampled CDL cropland were used as the cropland mask of the USA. For other area outside the USA, we chose the union of IGBP cropland and GlobeLand30 cultivated land as the cropland mask.

Rice maps around the world were collected for parameter selection and accuracy assessment (Supplementary Table 2), which may come from officially released data, previous studies, ground surveys, visual interpretation, etc. Rice maps were processed to the same format as 500 m MODIS tiles, consistent with NDVIs and LSWIs. When processing a rice map with spatial resolution much higher than 500 m (for example, 10 m), we first scan the whole image with a $L \times L$ detecting window to select vast pixels, that means, fragmentary pixels which are not inside any detecting window would be excluded. L denotes the length of detecting window. Then, we resampled the scanned high-resolution image to 500 m, labeled 500 m pixels with rice proportion more than 50% as rice. For rice probability surface map in Australia, we used PhenoRice⁵⁰ algorithm to select highly reliable rice pixels. Moreover, for calibration and validation, we obtained country-level statistics from Food and Agriculture Organizations of the United Nations (FAO).

The global seamless 1 km daily land surface temperature (LST) dataset in 2003–2020³⁶ was adopted to analyze the cooling effect of paddy fields, which contains daytime (13:30) LST and nighttime (01:30) LST. The Digital Elevation Model (DEM) dataset incorporated to improve the reliability of calculation of cooling effect. The DEM dataset we used was Global Version Elevation (GVE). Both the LST and DEM datasets were resampled to the 500 m MODIS tile format for consistency with GlobalRice500.

Rice mapping framework

The MPD_DTW framework (Fig. 1) consists of two core modules: Moving Phenological Detection (MPD) and Dynamic Time Warping (DTW). The MPD module detects the start of the season (SOS) and end of season (EOS) of the rice growing season on a daily, pixel-by-pixel basis. SOS is identified based on the flooding criterion (Eq. 3).

$$\text{LSWI} + F > \text{NDVI} \quad (3)$$

where F represents the flood factor. This process continues daily until $\text{LSWI} + F$ exceeds NDVI, marking the onset of transplanting and thus defining the SOS. Following this, MPD identifies EOS when a local minimum of NDVI is detected, indicating a significant decline in biomass and greenness after harvest. EOS detection is further constrained such that

$$\text{EOS} - \text{SOS} \in [T_1, T_2] \quad (4)$$

where T_1 and T_2 denote the lower and upper bounds of the locally defined rice growth duration. If no day satisfies the conditions of EOS within this expected time window, the module resumes the search for the next SOS.

Once an SOS and an EOS are established, the NDVI curve from this interval is analyzed through the DTW module. This module calculates the dissimilarity between the detected NDVI curve and a predefined standard rice NDVI curve derived from the collected reference rice maps. To accommodate the variability in the lengths of rice growing seasons, we employed the classic curve-alignment algorithm DTW to compute the dissimilarity. DTW nonlinearly aligns two time series of varying lengths to find the optimal warping path^{51,52}. The cost of the optimal alignment can be recursively computed by

$$D(A_i, R_j) = \delta(a_i, r_j) + \min \begin{cases} D(A_{i-1}, R_{j-1}) \\ D(A_i, R_{j-1}) \\ D(A_{i-1}, R_j) \end{cases} \quad (5)$$

where $A_i = \langle a_1, \dots, a_i \rangle$ is the subsequence of the NDVI curve of an observed pixel within the identified SOS–EOS period, and $R_j = \langle r_1, \dots, r_j \rangle$ is the subsequence of a standard rice NDVI curve. The DTW dissimilarity is then given by the distance at the end of the alignment, $D(A, R)$, which reflects the overall similarity in biomass and greenness dynamics between observed pixels and standard rice phenology.

If the DTW dissimilarity falls below a predefined threshold, current NDVI curve would be classified as a rice curve. And the detection of SOS will immediately skip to the identified EOS, ensuring no overlaps between different rice growing seasons. If the dissimilarity failed to satisfy the condition, the detection of SOS would continue at the day after current SOS.

Accuracy assessments of rice mapping

To evaluate mapping performance, two approaches were used. One is to precisely compute accuracies in reference regions where rice samples are present, the other is to compare mapped areas with statistical data across all subregions where official statistics are available.

Producer’s Accuracy (PA), User’s Accuracy (UA), Overall Accuracy (OA) and F1 score were used for accuracy assessment in reference regions. The corresponding formulas are as follows:

$$PA = \frac{TP}{TP + FN} \quad (6)$$

$$UA = \frac{TP}{TP + FP} \quad (7)$$

$$OA = \frac{TP + TN}{TP + FN + FP + TN} \quad (8)$$

$$F1 = \frac{2 \times UA \times PA}{UA + PA} \quad (9)$$

where TP denotes true positives (i.e., rice correctly predicted as rice), TN stands for true negatives (i.e., non-rice correctly predicted as non-rice), FP represents false positives (i.e., non-rice incorrectly predicted as rice), and FN refers to the false negatives (i.e., rice incorrectly predicted as non-rice).

Country-level validation was performed against FAO statistics. For each country and year, we aggregated the pixel-level satellite-derived results into harvested area by summing the area of all pixels mapped as harvested and counting distinct harvest events within the calendar year (i.e., a pixel harvested k times contributes $k \times$ pixel area). This aggregation matches the spatial and temporal scales of the FAO data. Specifically, the relative errors (δ) between mapped areas and

statistical areas were computed:

$$\delta = \frac{\text{Area}_{\text{map},k,c} - \text{Area}_{\text{stat},k,c}}{\text{Area}_{\text{stat},k,c}} \times 100\% \quad (10)$$

where k denotes year, c represents country, Area_{map} means the harvest areas from mapping results and $\text{Area}_{\text{stat}}$ refers to the harvest areas from statistics.

Measuring cooling effect of paddy fields

The ΔLST was used to quantify the cooling effect of paddy fields, which represents the difference in LST between surrounding non-paddy cropland and paddy fields during the growing seasons (Eq. 11).

$$\Delta\text{LST} = \text{LST}_{\text{non-paddy}} - \text{LST}_{\text{paddy}} \quad (11)$$

where $\text{LST}_{\text{paddy}}$ and $\text{LST}_{\text{non-paddy}}$ denote the mean LST of paddy and non-paddy areas, respectively. Unless specified, LST refers to the mean LST during the rice growing season. In the calculation of the mean value of LST, we excluded data below the 5th percentage and above the 95th percentage to mitigate the impact of outliers.

To enhance comparability and reduce uncertainty, the non-paddy areas were selected under the following constraints^{8,11,35}: (1) non-paddy pixels were selected exclusively from cropland to mitigate disturbances from the underlying surfaces; (2) the paddy and non-paddy fields cannot be too distant from each other to ensure similar climatic conditions. We established a maximum allowable distance of 20 km between paddy and non-paddy fields; (3) elevation differences between paddy and non-paddy fields should be controlled to reduce temperature variations caused by changes in elevation. In our study, all elevation differences were less than 50 m; (4) the number of non-paddy pixels needs to be sufficiently large, reducing random errors. In our analysis, at least 10 non-paddy pixels were included in each comparison.

To analyze the relationship between ΔLST and paddy proportion, the paddy proportion refers to the percentage of paddy rice within a grid composed of 20 pixels \times 20 pixels (approximately 10 km \times 10 km). All 10 km \times 10 km grids across the globe are binned based on paddy proportion, with each bin representing a 1% interval. For example, bin k represents all grids where paddy proportion in the range ($k-1\%$, $k\%$). The mean ΔLST during 2003–2020 of each bin is used as the representative ΔLST for that bin. Grids with a paddy proportion smaller than 0.2 were excluded, as the irradiance effect can be better observed when vegetation fraction is higher than 0.2^{53,54}.

To represent non-paddy areas at different locations, the non-paddy ladder (NPL) was defined. Specifically, NPL_d refers to the set of non-paddy pixels within a square-shaped ring with a distance of d pixels from the edge of the paddy field (Supplementary Fig. 1a). NPL_{d1-d2} denotes the non-paddy pixels located within a square-shaped annular area between $d1$ and $d2$ pixels from the edge of the paddy field (Supplementary Fig. 1b). Please note that the distances described in the subscripts are measured in units of MODIS pixels (\sim 500 m).

In this study, if no specific NPL is indicated, the “non-paddy” in $\text{LST}_{\text{non-paddy}}$ default to NPL_{10-30} . NPL_{10-30} was chosen instead of NPL_{0-30} (excluding NRL_{0-9}). When examining the ΔLST across different non-paddy ladders (NPLs), non-paddy area in $\text{LST}_{\text{non-paddy}}$ is specified as a particular NPL_d (Supplementary Fig. 1c). For example, In the x-axis of Figs. 2, 3 represents NPL_3 , i.e., NPL_{3-4} .

Uncertainty analysis of ΔLST

For ΔLST estimates at 500 m resolution, we quantified their uncertainty using a block bootstrap^{55,56} procedure, to account for both spatial and temporal autocorrelation. Each bootstrap sampling unit was defined as the combination of a spatial block (64 \times 64 pixels, \sim 32 \times 32 km) and a temporal unit (one calendar year). The ΔLST mean

was recalculated for each bootstrap replicate. Based on 10,000 replicates, the standard errors of the mean (SEMs) and 95% confidence intervals (95% CIs) were derived from the bootstrap distributions. For the paddy-proportion-based means (Fig. 5a), the data had already been aggregated to 20 × 20 pixels; therefore, uncertainty was assessed directly using a Student's *t* test. The “±” values reported throughout this paper represent the standard error of the mean (SEM) unless otherwise specified.

Data availability

The GlobalRice500³¹ dataset generated in this study have been deposited in the Zenodo database (<https://doi.org/10.5281/zenodo.17460919>). The mean values and uncertainty quantification underlying the Figures generated in this study are provided in the Supplementary Information and Source Data file. Publicly available data used in this study are referenced. Source data are provided with this paper.

Code availability

The MPD_DTW³⁰ code is available at <https://doi.org/10.5281/zenodo.17679402>. The source code is freely available for non-commercial research and educational purposes, provided that proper attribution is given. Modification and redistribution are permitted under the same conditions. Commercial use of the software is strictly prohibited.

References

1. Yuan, S. et al. Sustainable intensification for a larger global rice bowl. *Nat. Commun.* **12**, 7163 (2021).
2. Qian, H. et al. Greenhouse gas emissions and mitigation in rice agriculture. *Nat. Rev. Earth Environ.* **4**, 716–732 (2023).
3. Null, N., Jensen, M. E. & Allen, R. G. *Evaporation, Evapotranspiration, and Irrigation Water Requirements*. <https://doi.org/10.1061/9780784414057> (American Society of Civil Engineers, 2016).
4. Chen, Z., Balasus, N., Lin, H., Nesser, H. & Jacob, D. J. African rice cultivation linked to rising methane. *Nat. Clim. Change* <https://doi.org/10.1038/s41558-023-01907-x> (2024).
5. Yan, X., Akiyama, H., Yagi, K. & Akimoto, H. Global estimations of the inventory and mitigation potential of methane emissions from rice cultivation conducted using the 2006 Intergovernmental Panel on Climate Change Guidelines. *Glob. Biogeochem. Cycles* **23**, GB2002 (2009).
6. Zhang, G. et al. Fingerprint of rice paddies in spatial–temporal dynamics of atmospheric methane concentration in monsoon Asia. *Nat. Commun.* **11**, 554 (2020).
7. Nikolaisen, M. et al. Methane emissions from rice paddies globally: a quantitative statistical review of controlling variables and modeling of emission factors. *J. Clean. Prod.* **409**, 137245 (2023).
8. Li, Y. et al. Biophysical impacts of earth greening can substantially mitigate regional land surface temperature warming. *Nat. Commun.* **14**, 121 (2023).
9. Alkama, R. et al. Vegetation-based climate mitigation in a warmer and greener World. *Nat. Commun.* **13**, 606 (2022).
10. Li, Y. et al. Observed different impacts of potential tree restoration on local surface and air temperature. *Nat. Commun.* **16**, 2335 (2025).
11. Li, Y. et al. Local cooling and warming effects of forests based on satellite observations. *Nat. Commun.* **6**, 6603 (2015).
12. Alkama, R. & Cescatti, A. Biophysical climate impacts of recent changes in global forest cover. *Science* **351**, 600–604 (2016).
13. Gillner, S., Vogt, J., Tharang, A., Dettmann, S. & Roloff, A. Role of street trees in mitigating effects of heat and drought at highly sealed urban sites. *Landsc. Urban Plan.* **143**, 33–42 (2015).
14. Li, G. et al. Global urban greening and its implication for urban heat mitigation. *Proc. Natl. Acad. Sci. USA* **122**, e2417179122 (2025).
15. Bonfils, C. & Lobell, D. Empirical evidence for a recent slowdown in irrigation-induced cooling. *Proc. Natl. Acad. Sci. USA* **104**, 13582–13587 (2007).
16. Thiery, W. et al. Warming of hot extremes alleviated by expanding irrigation. *Nat. Commun.* **11**, 290 (2020).
17. Bo, Y. et al. Improved alternate wetting and drying irrigation increases global water productivity. *Nat. Food* **5**, 1005–1013 (2024).
18. Yokohari, M., Brown, R. D., Kato, Y. & Yamamoto, S. The cooling effect of paddy fields on summertime air temperature in residential Tokyo, Japan. *Landsc. Urban Plan.* **53**, 17–27 (2001).
19. Liu, W. et al. Biophysical effects of paddy rice expansion on land surface temperature in Northeastern Asia. *Agric. For. Meteorol.* **315**, 108820 (2022).
20. Xue, W., Jeong, S., Ko, J. & Yeom, J.-M. Contribution of biophysical factors to regional variations of evapotranspiration and seasonal cooling effects in Paddy Rice in South Korea. *Remote Sens.* **13**, 3992 (2021).
21. Portmann, F. T., Siebert, S. & Döll, P. MIRCA2000—Global monthly irrigated and rainfed crop areas around the year 2000: A new high-resolution data set for agricultural and hydrological modeling. *Glob. Biogeochem. Cycles* **24**, 2008GB003435 (2010).
22. Grogan, D., Froliking, S., Wisser, D., Prusevich, A. & Glidden, S. Global gridded crop harvested area, production, yield, and monthly physical area data circa 2015. *Sci. Data* **9**, 15 (2022).
23. Tang, F. H. M. et al. CROPGRIDS: a global geo-referenced dataset of 173 crops. *Sci. Data* **11**, 413 (2024).
24. Leff, B., Ramankutty, N. & Foley, J. A. Geographic distribution of major crops across the world. *Glob. Biogeochem. Cycles* **18**, GB1009 (2004).
25. Iizumi, T. & Sakai, T. The global dataset of historical yields for major crops 1981–2016. *Sci. Data* **7**, 97 (2020).
26. Iizumi, T. et al. Uncertainties of potentials and recent changes in global yields of major crops resulting from census- and satellite-based yield datasets at multiple resolutions. *PLOS ONE* **13**, e0203809 (2018).
27. Iizumi, T. et al. Historical changes in global yields: major cereal and legume crops from 1982 to 2006. *Glob. Ecol. Biogeogr.* **23**, 346–357 (2014).
28. Carrasco, L., Fujita, G., Kito, K. & Miyashita, T. Historical mapping of rice fields in Japan using phenology and temporally aggregated Landsat images in Google Earth Engine. *ISPRS J. Photogramm. Remote Sens.* **191**, 277–289 (2022).
29. Jo, H.-W. et al. Recurrent U-Net based dynamic paddy rice mapping in South Korea with enhanced data compatibility to support agricultural decision making. *GIScience Remote Sens.* **60**, 2206539 (2023).
30. Weng, W. MPD_DTW. Zenodo <https://doi.org/10.5281/ZENODO.17679402> (2025).
31. Weng, W. GlobalRice500. Zenodo <https://doi.org/10.5281/ZENODO.17460918> (2025).
32. Chiueh, Y.-W., Tan, C.-H. & Hsu, H.-Y. The value of a decrease in temperature by one degree celsius of the regional microclimate—The cooling effect of the paddy field. *Atmosphere* **12**, 353 (2021).
33. Yang, M. et al. Mitigating urban heat island through neighboring rural land cover. *Nat. Cities* **1**, 522–532 (2024).
34. Martilli, A., Krayerhoff, E. S. & Nazarian, N. Is the Urban Heat Island intensity relevant for heat mitigation studies?. *Urban Clim.* **31**, 100541 (2020).
35. Lee, X. et al. Observed increase in local cooling effect of deforestation at higher latitudes. *Nature* **479**, 384–387 (2011).
36. Zhang, T., Zhou, Y., Zhu, Z., Li, X. & Asrar, G. R. A global seamless 1 km resolution daily land surface temperature dataset (2003–2020). *Earth Syst. Sci. Data* **14**, 651–664 (2022).

37. Wan, Z. New refinements and validation of the collection-6 MODIS land-surface temperature/emissivity product. *Remote Sens. Environ.* **140**, 36–45 (2014).
38. Rubel, F., Brugger, K., Haslinger, K. & Auer, I. The climate of the European Alps: shift of very high resolution Köppen-Geiger climate zones 1800–2100. *Meteorol. Z.* **26**, 115–125 (2017).
39. Wang, H., Yue, C. & Luyssaert, S. Reconciling different approaches to quantifying land surface temperature impacts of afforestation using satellite observations. *Biogeosciences* **20**, 75–92 (2023).
40. IPCC. Climate Change 2021 – The Physical Science Basis. (Cambridge University Press, 2023). <https://doi.org/10.1017/9781009157896>
41. Kritee, K. et al. High nitrous oxide fluxes from rice indicate the need to manage water for both long- and short-term climate impacts. *Proc. Natl. Acad. Sci. USA* **115**, 9720–9725 (2018).
42. FAO. FAOSTAT Statistical Database. <https://www.fao.org/faostat/> (accessed 10 Sep 2024).
43. Bright, R. M. et al. Local temperature response to land cover and management change driven by non-radiative processes. *Nat. Clim. Change* **7**, 296–302 (2017).
44. Zeng, Z. et al. Climate mitigation from vegetation biophysical feedbacks during the past three decades. *Nat. Clim. Change* **7**, 432–436 (2017).
45. Zhang, X. et al. Monitoring vegetation phenology using MODIS. *Remote Sens. Environ.* **84**, 471–475 (2003).
46. Chandrasekar, K., Sesha Sai, M. V. R., Roy, P. S. & Dwevedi, R. S. Land Surface Water Index (LSWI) response to rainfall and NDVI using the MODIS Vegetation Index product. *Int. J. Remote Sens.* **31**, 3987–4005 (2010).
47. Huang, J., Wang, X. & Wang, F. *Uncertainty in Paddy Rice Remote Sensing* (Zhejiang University Press, 2013).
48. Chen, J. et al. A simple method for reconstructing a high-quality NDVI time-series data set based on the Savitzky–Golay filter. *Remote Sens. Environ.* **91**, 332–344 (2004).
49. Chen, J. et al. Global land cover mapping at 30m resolution: A POK-based operational approach. *ISPRS J. Photogramm. Remote Sens.* **103**, 7–27 (2015).
50. Boschetti, M. et al. PhenoRice: a method for automatic extraction of spatio-temporal information on rice crops using satellite data time series. *Remote Sens. Environ.* **194**, 347–365 (2017).
51. Sakoe, H. & Chiba, S. Dynamic programming algorithm optimization for spoken word recognition. *IEEE Trans. Acoust. Speech Signal Process.* **26**, 43–49 (1978).
52. Petitjean, F., Inglada, J. & Gancarski, P. Satellite Image Time Series Analysis Under Time Warping. *IEEE Trans. Geosci. Remote Sens.* **50**, 3081–3095 (2012).
53. Hou, M., Hu, Y. & He, Y. Modifications in vegetation cover and surface albedo during rapid urbanization: a case study from South China. *Environ. Earth Sci.* **72**, 1659–1666 (2014).
54. Yang, J. et al. Characterizing the thermal effects of vegetation on urban surface temperature. *Urban Clim.* **44**, 101204 (2022).
55. Burke, M., Hsiang, S. M. & Miguel, E. Global non-linear effect of temperature on economic production. *Nature* **527**, 235–239 (2015).
56. Moore, F. C., Baldos, U., Hertel, T. & Diaz, D. New science of climate change impacts on agriculture implies higher social cost of carbon. *Nat. Commun.* **8**, 1607 (2017).
57. Han, J. et al. NESEA-Rice10: high-resolution annual paddy rice maps for Northeast and Southeast Asia from 2017 to 2019. *Earth Syst. Sci. Data* **13**, 5969–5986 (2021).
58. Sun, C. et al. Twenty-meter annual paddy rice area map for mainland Southeast Asia using Sentinel-1 synthetic-aperture-radar data. *Earth Syst. Sci. Data* **15**, 1501–1520 (2023).
59. USDA National Agricultural Statistics Service. Cropland Data Layer. USDA-NASS.

Acknowledgements

This research has been financially supported by the National Natural Science Foundation of China (No. 42171314) and the National Key Research and Development Program (No. 2023YFD2300300).

Author contributions

J.H. proposed the research idea. W.W. and J.H. designed the research. W.W. led the experiments and wrote the first draft. C.Y. provided theoretical guidance. Z.L., S.L., R.H., and F.B. contributed to data collection. W.W. and Z.L. performed data preprocessing. Y.X. provided technical support. Y.X., D.P., C.H., L.L., and W. L. contributed to the interpretation and the preparation of the manuscript. W.W., C.Y., and J.H. led the revisions. All authors reviewed and approved the final paper.

Competing interests

The authors declare no competing interests.

Additional information

Supplementary information The online version contains supplementary material available at <https://doi.org/10.1038/s41467-025-67549-z>.

Correspondence and requests for materials should be addressed to Jingfeng Huang.

Peer review information *Nature Communications* thanks Anne Gobin and the other, anonymous, reviewer for their contribution to the peer review of this work. A peer review file is available.

Reprints and permissions information is available at <http://www.nature.com/reprints>

Publisher's note Springer Nature remains neutral with regard to jurisdictional claims in published maps and institutional affiliations.

Open Access This article is licensed under a Creative Commons Attribution-NonCommercial-NoDerivatives 4.0 International License, which permits any non-commercial use, sharing, distribution and reproduction in any medium or format, as long as you give appropriate credit to the original author(s) and the source, provide a link to the Creative Commons licence, and indicate if you modified the licensed material. You do not have permission under this licence to share adapted material derived from this article or parts of it. The images or other third party material in this article are included in the article's Creative Commons licence, unless indicated otherwise in a credit line to the material. If material is not included in the article's Creative Commons licence and your intended use is not permitted by statutory regulation or exceeds the permitted use, you will need to obtain permission directly from the copyright holder. To view a copy of this licence, visit <http://creativecommons.org/licenses/by-nc-nd/4.0/>.

© The Author(s) 2025